

OXYGEN PUMPING II: PROBING THE INHOMOGENEOUS METAL ENRICHMENT AT THE EPOCH OF REIONIZATION WITH HIGH FREQUENCY CMB OBSERVATIONS

CARLOS HERNÁNDEZ-MONTEAGUDO¹, ZOLTÁN HAIMAN², LICIA VERDE,^{3,4} AND RAUL JIMENEZ^{3,4}

Draft version November 2, 2018

ABSTRACT

At the epoch of reionization, when the high-redshift inter-galactic medium (IGM) is being enriched with metals, the $63.2\mu\text{m}$ fine structure line of OI is pumped by the $\sim 1300\text{\AA}$ soft UV background and introduces a spectral distortion in the Cosmic Microwave Background (CMB). Here we use a toy model for the spatial distribution of neutral oxygen, assuming metal bubbles surround dark matter halos, and compute the fluctuations of this distortion, and the angular power spectrum it imprints on the CMB. We discuss the dependence of the power spectrum on the velocity of the winds polluting the IGM with metals, the minimum mass of the halos producing these winds, and on the cosmic epoch when the OI pumping occurs. We find that, although the clustering signal of the CMB distortion is weak ($(\delta y)_{rms} \lesssim 10^{-7}$) (roughly corresponding to a temperature anisotropy of $\sim \text{nK}$), it may be reachable in deep integrations with high-sensitivity infrared detectors. Even without a detection, these instruments should be able to useful constraints on the heavy element enrichment history of the IGM.

Subject headings: cosmology: cosmic microwave background - cosmology : theory - galaxies: intergalactic medium - atomic processes

1. INTRODUCTION

Probing the Dark Ages – the epoch between the last scattering surface of the CMB at $z \sim 1000$ and the completion of the reionization of the IGM at $z \sim 6$, including the formation of the first luminous objects – constitutes the next frontier of observational cosmology. Among the major open questions are the nature of the objects that reionized the universe, and the origin of the first heavy elements, as well as the efficiency with which they were mixed into the high-redshift IGM.

To date, the reionization history has been constrained by observations of Lyman series absorption spectra of $z \sim 6$ quasars (see Fan et al. 2006 for a recent review) by GRB observations at high redshifts (Totani et al. 2006), by observations of Lyman- α selected galaxies (Kashikawa et al. 2006; McQuinn et al. 2007; Dijkstra et al. 2007; Malhotra & Rhoads 2006) and by CMB polarization anisotropies (Kogut et al. 2003; Page et al. 2007; Spergel et al. 2007). The present constraints, however, are consistent with a wide range of scenarios, and considerable theoretical and experimental effort is devoted to developing new probes of the high-redshift universe. A promising possibility is to use the redshifted 21cm hyperfine line of HI (see Furlanetto et al. (2006) and references therein). Metal enrichment of the high-redshift IGM may be another useful tracer of the reionization process. For example Basu et al. (2004) and Hernández-Monteagudo et al. (2006) considered the elastic resonant scattering of CMB photons by intergalac-

tic metals. Recent studies have focused, in particular, on the detectability of neutral oxygen (OI; Oh 2002; Basu et al. 2004), as this element is thought to be produced in abundance by the first stars (Heger & Woosley 2002). Scattering of UV photons by OI, and the corresponding absorption features in the spectra of quasars – the OI forest – was proposed as a possible observable by Oh (2002), and may have recently been detected at $z \sim 6$ (Becker et al. 2006). Since OI and HI are in charge exchange equilibrium, oxygen is likely to be highly ionized in regions where hydrogen is actively ionized. However, the recombination time for oxygen is shorter than the Hubble time, and it can be neutral even in “fossil” HII regions where hydrogen had been ionized, but where short-lived ionizing sources have turned off, allowing the region to recombine (Oh 2002). Oh & Haiman (2003) show that the filling factor of such fossil HII regions can be large ($\gtrsim 50\%$) prior to reionization.

In a previous paper (Hernández-Monteagudo et al. 2007; hereafter Paper I), we showed that the $63.2\mu\text{m}$ fine structure line of neutral OI can be pumped by the $\sim 1300\text{\AA}$ soft UV background, via the Balmer α line of OI. This is analogous to the Wouthuysen-Field effect for exciting the 21cm line of cosmic HI. In Paper I, we found that OI at redshift z should be seen in emission at $(1+z)63.2\mu\text{m}$, and for $7 < z < 10$ it would produce a mean spectral distortion of the CMB with a y -parameter of $y \equiv \Delta I_\nu / B_\nu [T_{CMB}] = (10^{-9} - 3 \times 10^{-8})(Z/10^{-3}Z_\odot)(I_{UV}/10)$, where Z is the mean metallicity of the IGM and I_{UV} is the UV background intensity at 1300\AA in units of $10^{-21} \text{ erg/s/Hz/cm}^2/\text{sr}$. In principle, this distortion could be detectable through a precise future measurement of the CMB spectrum (see Fixsen & Mather 2002 for the prospects of such measurements), and would then open the possibility of performing tomography of the metal distribution. In combination with HI 21cm studies, it could yield direct measurements of the abundance and spatial distribution of

¹ Department of Physics and Astronomy, University of Pennsylvania, Philadelphia, PA 19104, USA; carloshm@astro.upenn.edu

² Department of Astronomy, Columbia University, 550 West 120th Street, New York, NY 10027, USA; haiman@astro.columbia.edu

³ Institute of Space Sciences (CSIC-IEEC)/ICREA, Campus UAB, Bellaterra 08193, Spain

⁴ Department of Astrophysical Sciences, Peyton Hall, Princeton University, Princeton NJ-08544, USA; raulj.lverde@astro.princeton.edu

metals in the high-redshift IGM.

Since oxygen pollution at high-redshift is likely associated with most over-dense regions in the IGM, hosting the first star forming activity, there must be spatial fluctuations in the OI abundance, causing fluctuations in the corresponding y distortion. In this paper, we consider the clustering properties of this signal. In particular, we use toy-models to describe the metal distribution, and compute the two-dimensional angular power spectrum of the CMB intensity. This would be appropriate for an instrument with a single (or a few discrete) frequency bands that probes the metals in a single (or a few discrete) narrow redshift bins. We find that the clustering signal induced by the inhomogeneous OI pumping is small, but possibly detectable with forthcoming instruments, e.g., with deep integrations (for 2-3 months) with the full ALMA array. A detection of the metal enrichment during the Dark Ages would be complementary to HI 21cm studies, and would provide clues about the distribution of metals in the IGM before galaxy formation started in full.

The rest of this paper is organized as follows. In § 2, we discuss the basics of the OI pumping process. In § 3, we outline the computation of the distortion induced by OI pumping along a given line of sight in the CMB. In § 4, we discuss our method to compute the angular power spectrum of the distortion, with the basic assumption that metals trace the distribution of collapsed halos. In § 5, we introduce toy models to describe the spatial distribution of metals, with the basic assumption that metals cluster around dark matter halos. In § 6, we present our main result on the angular power spectrum, and discuss its dependence on the basic model parameters, as well as its detectability. Finally, in § 7, we summarize the implications of this work and offer our conclusions. Throughout this paper, we adopt a set of “concordance” cosmological parameters for a flat universe, $\Omega_m = 0.29$, $\Omega_\Lambda = 0.71$, $\Omega_b = 0.047$, $h = 0.72$, with a power spectrum normalization $\sigma_8 = 0.75$ and slope $n = 0.99$.

2. THE BALMER- α PUMPING OF OI

In Paper I, we computed the distortion in the CMB induced by neutral oxygen in environments where UV radiation is pumping the fine structure 63.2 μm M1 transition (between the $n = 2$ electronic states 3P_2 and 3P_1) via the Balmer- α line at $\sim 1302\text{\AA}$ connecting these two states with the excited $n = 3$ electronic state 3S_1 . In what follows, we shall denote the 3P_2 and 3P_1 states as “0” and “1” respectively, and the excited state 3S_1 as “2”. Energy and frequency differences between levels will be denoted as E_{ji} , ν_{ji} , with $i, j = 0, 1, 2$ and $j > i$.

In Paper I, we showed that this process of *Balmer α pumping* modifies the occupation of the levels 0 and 1 and therefore introduces a shift in the spin temperature T_S , so that it slightly departs from the CMB temperature, T_{CMB} . Since at reionization the UV background flux at ν_{10} is smaller than at ν_{21} , T_S will be above T_{CMB} , producing an excess of 63.2 μm photons. Each of these excess photons is generated by the sequence of three radiative transitions $0 \rightarrow 2 \rightarrow 1 \rightarrow 0$, i.e., a photon of frequency ν_{20} is broken into two photons of frequencies ν_{21} and ν_{10} .

In Paper I, we were interested in the average distortion

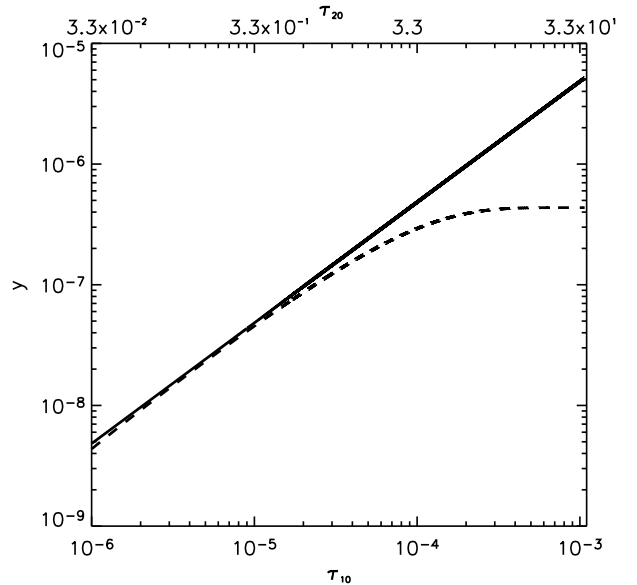


FIG. 1.— The distortion parameter y induced by the Balmer- α pumping of the OI 63.2 μm transition is shown as a function of the optical depths τ_{10} and τ_{20} at redshift $z = 7$. The optically thin solution presented in Paper I is shown as the solid curve, accurately describing the system at low and intermediate τ_{10} . When the $2 \leftrightarrow 0$ transition becomes optically thick ($\tau_{20} \sim 1$, corresponding to $\tau_{10} \sim 3 \times 10^{-5}$), the results are obtained by tracking the photon and level populations as dictated by equation (2), and shown by the dashed curve. Note that at low τ_{10} there is a slight mismatch between the solid and the dashed lines, caused by numerical error due to the finite size of our integration step.

over the full sky, and considered the optically thin limit for the Balmer- α transition. While this is justified if the OI is homogeneously distributed (in which case, $\tau_{20} \sim 0.01[Z/(10^{-2.5}Z_\odot)]$ and $\tau_{21} \ll 1$), here we will consider metal distributions that can be highly inhomogeneous. The metal-enriched bubbles can potentially contain a large concentration of metals and become optically thick at ν_{20} . For this reason, we consider the case $\tau_{20} \gtrsim 1$ and self-consistently solve the equations of radiative transfer to follow the UV intensity as the background radiation penetrates the OI-rich bubble.

The equations governing the evolution of the relative populations n_i (with $i = 0, 1$) and the number of photons at the frequencies n_ν^{2j} , $j = 1, 2$ are:

$$\frac{dn_0}{dt} = -n_0 \left[\frac{g_1}{g_0} A_{10} \frac{c^2 I_\nu^{10}}{2h\nu_{10}^3} + P_{01} \right] + n_1 A_{10} \left[1 + \frac{c^2 I_\nu^{10}}{2h\nu_{10}^3} + \frac{P_{10}}{A_{10}} \right], \quad (1)$$

$$\frac{dn_\nu^{20}}{dt} = c \frac{\lambda_{20}^2}{8\pi} \Psi_\nu \left[-P_{01}n_0 + P_{10}n_1 \right], \quad (2)$$

where Ψ_ν denotes the line profile, assumed to have a width corresponding to a thermally broadened line with $T_{OI} \sim 20$ eV (corresponding to a relative thermal width of $\sim 4 \times 10^{-5}$). For simplicity, we assume top-hat shapes for the line profiles, and we include the effect of cosmological redshift by adopting an appropriate effective length for the line-of-sight integral (discussed below). In addition, atom and photon number conservation imply that $dn_1/dt = -dn_0/dt$ and $dn_\nu^{21}/dt = -dn_\nu^{20}/dt$.

As initial conditions, we chose $T_S = T_{CMB}$, $I_\nu^{21} = 2 \times 10^{-20} \text{ erg cm}^{-2} \text{ s}^{-1} \text{ Hz}^{-1} \text{ sr}^{-1}$, and $I_\nu^{20}/I_\nu^{21} \simeq 1 - \beta$, with $\beta = 0.02$ as in Paper I (our results are largely insensitive to the choice of this parameter, as shown in Paper I). Figure 1 shows the result of evolving this system of equations at $z = 7$. At low τ_{10} , the results (dashed curve) coincide with the optically thin steady state solution of Paper I (solid curve) within a few percent level corresponding to inaccuracies in the numerical integration. At larger values of $\tau_{10} \gtrsim 10^{-4}$, the Balmer- α transition becomes optically thick and the number of available pumping UV photons decreases. As a result, once these photons are exhausted, the distortion y flattens out at the maximum value of $y \sim 3 \times 10^{-7}$.

3. THE SPECTRAL DISTORTIONS ON THE CMB

The total distortion introduced by OI in the CMB at a given observing frequency ν_{obs} is

$$y = \int dr (j_\nu/B_\nu[T_0])(r) \simeq \frac{j_\nu}{B_\nu[T_0]}(\nu_{obs}) \Delta r, \quad (3)$$

where j_ν is an effective emissivity which is non zero only at the redshift satisfying $1 + z_s \approx \nu_{10}/\nu_{obs}$ (see Paper I for more details). For a uniform OI distribution, and assuming that the OI atoms follow the Hubble expansion, the effective length Δr along which this emissivity is not zero is $cH^{-1}(z_s) (\Delta\nu_{th}/\nu_{10})$, where $\Delta\nu_{th}$ is the width of the line. However, if oxygen is clumped (for example, confined within bubbles) then the effective length Δr may vary. If the physical size L of the bubble is small, $L \lesssim cH^{-1}(z_s) (\Delta\nu_{th}/\nu_{10})$, then $\Delta r \approx L$. On the other hand, if $L \gtrsim cH^{-1}(z_s) (\Delta\nu_{th}/\nu_{10})$ and the bubble has split from the Hubble flow, then also $\Delta r = L$. But if the bubble is comoving with the Hubble flow, then $\Delta r = cH^{-1}(z_s) (\Delta\nu_{th}/\nu_{10})$, (this length, at $z = 7$, corresponds to $\sim 12 \text{ Kpc}$). Note that, unless otherwise stated, distances will always be in physical units (and not comoving). In this work, we shall assume that bubbles are not gravitationally bound, and for simplicity, we further assume that they expand with the Hubble flow, so that $\Delta r = \min(L, cH^{-1}(z_s) \Delta\nu_{th}/\nu_{10})$. Hence, in this case,

$$y \simeq \frac{j_\nu}{B_\nu[T_0]} \min\left(L, cH^{-1}(z_s) \frac{\Delta\nu_{th}}{\nu_{10}}\right). \quad (4)$$

Depending on the angular and spectral resolution of a specific instrument, the y -distortion along a given line-of-sight, and at a given frequency, may have to be convolved with the respective response functions (clearly, such smoothing can reduce the fluctuations). In what follows, we adopt a model instrumental beam (or PSF) response function $V_{psf}(\hat{\mathbf{n}})$ and a frequency response function $\Phi(\nu)$. Both will be taken to have accurately determined Gaussian shapes, so that $\int d\hat{\mathbf{n}} V_{psf}(\hat{\mathbf{n}}) = \int d\nu \Phi(\nu) = 1$, where $\hat{\mathbf{n}}$ denotes the unit vector.

We assume generically that each OI-bubble is associated with a halo of some mass M , with an abundance given by the Sheth-Tormen (ST, Sheth & Tormen 2004) mass function dn/dM , and that the OI atoms are distributed in a bubble around the halo with a spherically symmetric density profile $W_b(r)$; in this case, a second convolution, over the bubble density profile, is necessary.

If we neglect the peculiar velocities and internal motions of the bubbles, the effective distortion along the line of sight in direction $\hat{\mathbf{n}}$, and at frequency ν_{obs} , reads

$$y_{eff}(\nu_{obs}, \hat{\mathbf{n}}) = \int_0^\infty \int_{PSF} d\nu d\hat{\mathbf{n}} \Phi(\nu) V_{psf}(\hat{\mathbf{n}}) \int_{r_s - \Delta r/2}^{r_s + \Delta r/2} dr \times \int \int d\mathbf{y} dM \frac{dn}{dM}(\mathbf{y}, M) W_b(\mathbf{y} - \mathbf{r}) \frac{j_\nu}{B_\nu[T_0]} \quad (5)$$

where $\mathbf{r} = r\hat{\mathbf{n}}$. The distance r is centered at the resonant value $r_s \equiv r[z_s]$ and Δr corresponds to the effective length defined above. The integral over M counts OI bubbles around halos of various masses (above some minimum halo mass M_{min} , as discussed further in § 5 below), whereas the integrals over ν and $\hat{\mathbf{n}}$ describe the cosmological volume probed by the PSF and the spectral response of the detector. Let us change variables from frequencies and angles to spatial coordinates, and define the three-dimensional instrumental PSF, $\mathcal{B}(\mathbf{x} - \mathbf{r}_s) \equiv \Phi(\nu[x])(\nu_{obs}/r_s^2)(dz/dr(z))V_{psf}(\hat{\mathbf{n}})^5$. Further defining $\hat{y}(M, z) \equiv (j_\nu/B_\nu[T_0])\Delta r$, the distortion generated by a bubble around a single halo of mass M at redshift z , we can re-write equation (5) more transparently as

$$y_{eff}(\nu_{obs}, \hat{\mathbf{n}}) \approx \int dM \left[\mathcal{B} \star \left(\frac{dn}{dM} \star W_b \right) \right] \hat{y}. \quad (6)$$

where \star denotes convolution. In what follows, the twice convolved halo number density will be denoted by \tilde{n} , i.e., $\tilde{n}(M, \mathbf{r}_s) \equiv [\mathcal{B} \star (dn/dM \star W_b)](M, \mathbf{r}_s)$.

Finally, the physical collision between two metal-rich bubbles will lead to a complicated thermo-dynamical interaction. Rather than modeling this process, the above prescription assumes a linear addition of the OI density (or y -distortion) from two physically overlapping metal bubbles. This simple assumption at least captures the enhancement of the metallicity in the overlap regions. We note that this is different from the case of merging HII bubbles during reionization, when mergers conserve volume and result in the expansion of the joint bubble.

4. THE EFFECT OF CLUSTERING

We next compute the second order moments (correlation function and power spectrum) of the distortion field generated by OI at $63.2\mu\text{m}$ during reionization. Throughout this discussion, we will consider a fixed redshift, and suppress the frequency-dependence of $y_{eff}(\hat{\mathbf{n}})$. The angular correlation function can be written as

$$\begin{aligned} \langle y_{eff}(\hat{\mathbf{n}}_1) y_{eff}(\hat{\mathbf{n}}_2) \rangle &= \int dM_1 dM_2 \langle \tilde{n}_1 \tilde{n}_2 \rangle \hat{y}_1 \hat{y}_2 \\ &= \int dM_1 dM_2 \tilde{n}_1 \tilde{n}_2 \hat{y}_1 \hat{y}_2 \left(1 + \tilde{\xi}_{hh}(\mathbf{r}_1, M_1, \mathbf{r}_2, M_2) \right). \end{aligned} \quad (7)$$

In this equation, \tilde{n} denotes *average* \tilde{n} . The correlation function $\tilde{\xi}_{hh}(\mathbf{r}_1, M_1, \mathbf{r}_2, M_2)$ corresponds to the halo-halo correlation function convolved with *both* the window function of the profile of the OI distribution (W_b) and the window function of the experiment (\mathcal{B}). Keeping in mind

⁵ The integral $\int d\mathbf{x} \mathcal{B}(\mathbf{x} - \mathbf{r}_s) = 1$ is normalized to unity in the volume centered at \mathbf{r}_s .

that the Fourier counterpart of ξ_{hh} is the matter power spectrum times the square of the bias factor $b(M, z)$ computed in Sheth & Tormen (1999), equation (7) becomes

$$\langle y_{eff}(\hat{\mathbf{n}}_1) y_{eff}(\hat{\mathbf{n}}_2) \rangle = \int dM_1 dM_2 \bar{n}_1 \bar{n}_2 \hat{y}_1 \hat{y}_2 b_1 b_2 \times \int \frac{d\mathbf{k}}{(2\pi)^3} P_m(k, z_{rs}) |\mathcal{B}_{\mathbf{k}}|^2 |W_{b,\mathbf{k}}|^2 \exp(-i\mathbf{k}(\mathbf{r}_1 - \mathbf{r}_2)), \quad (8)$$

with $P_m(k, z_s)$ the matter power spectrum at redshift z_s , (note that we have dropped a constant $-k=0$ - term and hence we are looking at the *departure* of the correlation function from its mean value) and $W_{b,\mathbf{k}}$ and $\mathcal{B}_{\mathbf{k}}$ the Fourier counterparts of W_b and \mathcal{B} respectively. Since we are assuming that every halo is producing a bubble, and the dominant signal will be due to the clustering of different bubbles, we can neglect non-linear corrections to the matter power spectrum. Such non-linear corrections would boost the clustering signals we predict below, but only on comoving scales of $\lesssim 0.1$ Mpc at $z \approx 6$ (e.g. Iliev et al. 2003), which is well below the scale at which the OI clustering signal peaks. The integral on \mathbf{k} can be split into a transverse (\mathbf{k}_\perp) and a parallel (k_z) component along the line of sight. We assume that both $\mathcal{B}_{\mathbf{k}}$, $W_{b,\mathbf{k}}$ can be factorised as $\mathcal{B}_{\mathbf{k}} = (\mathcal{B}_{\mathbf{k}_\perp} \mathcal{B}_{k_z})$ and $W_{b,\mathbf{k}} = (W_{b,\mathbf{k}_\perp} W_{b,k_z})$. For a Gaussian instrumental response, we can write $\mathcal{B}_{\mathbf{k}_\perp} = \exp[-k_\perp^2(r_s \sigma_b)^2/2]$ and $\mathcal{B}_{k_z} = \exp[-k_z^2((dr(z)/dz)\sigma_\nu/\nu_{obs})^2/2]$, with σ_b related to the width of the angular PSF and σ_ν to the width of $\Phi(\nu)$. For simplicity, the bubble is taken to have a Gaussian profile and a volume equal to $(\sqrt{2\pi}L)^3$. After this decomposition, the correlation function reads

$$\langle y_{eff}(\hat{\mathbf{n}}_1) y_{eff}(\hat{\mathbf{n}}_2) \rangle = \int \frac{d\mathbf{k}_\perp}{(2\pi)^2} \exp(-i\mathbf{k}_\perp(\mathbf{r}_1 - \mathbf{r}_2)_\perp) \int dM_1 dM_2 \bar{n}_1 \bar{n}_2 \hat{y}_1 \hat{y}_2 b_1 b_2 \times |\mathcal{B}_{\mathbf{k}_\perp} W_{b,\mathbf{k}_\perp}|^2 \int \frac{dk_z}{2\pi} |\mathcal{B}_{k_z} W_{b,k_z}|^2 P_m(k_\perp, k_z, z_{rs}). \quad (9)$$

Finally, by noting that in the flat sky approximation $\mathbf{k}_\perp \simeq 1/r_s$, we obtain the angular power spectrum:

$$C_l = \frac{1}{r_s^2} \int \int dM_1 dM_2 \bar{n}_1 \bar{n}_2 \hat{y}_1 \hat{y}_2 b_1 b_2 |\mathcal{B}_{1/r_s} W_{b,1/r_s}|^2 \int \frac{dk_z}{2\pi} |\mathcal{B}_{k_z} W_{b,k_z}|^2 P_m(1/r_s, k_z, z_s). \quad (10)$$

Let us briefly examine the behaviour of the C_l 's. We first recall that the Fourier window function of a bubble is proportional to the bubble volume ($\propto L^3$), and that the oxygen number density in bubbles is proportional to $\bar{n}_{OI}/(\bar{N}L^3)$, with \bar{N} the average bubble number density, \bar{n}_{OI} the global mean oxygen number density at a given redshift, and L the typical bubble size. We also note that the bias factor b almost cancels the redshift dependence of the growth factor of perturbations (e.g., Oh et al. 2003), so the scaling of the maximum of $l^2 C_l$ is $(l^2 C_l)_{max} \propto \mathcal{G}^2 \bar{n}_{OI}^2 (\Delta r)^2$, with \mathcal{G} a frequency-dependent function accounting for the efficiency of the pumping process and Δr the effective length in equation (3). \mathcal{G} dominates the overall redshift dependence

of the power spectrum amplitude. If L is smaller than $cH^{-1}(z_s) \Delta\nu_{th}/\nu_{10}$, then $(l^2 C_l)_{max} \propto \mathcal{G}^2 \bar{n}_{OI}^2 L^2$, but otherwise $(l^2 C_l)_{max} \propto \mathcal{G}^2 \bar{n}_{OI}^2$, i.e., the band power spectrum is independent of the bubble size (except that the bubble Fourier window function suppresses power at scales smaller than the bubble size). In either case, note that $(l^2 C_l)_{max}$ is proportional to the square of the oxygen metallicity. However, if the OI abundance within the bubbles is so high that they become optically thick at ν_{20} , then y will reach its plateau, $y \sim \mathcal{G}$ and $(l^2 C_l)_{max} \propto \mathcal{G}^2 (\bar{N}L^2)^2$, i.e., $(l^2 C_l)_{max}$ will be proportional to the square of the number density of bubbles times their cross-sectional area, assuming that the frequency resolution of the instrument corresponds to a radial distance that does not exceed the typical bubble size. Otherwise the scaling would be $(l^2 C_l)_{max} \propto \mathcal{G}^2 (\bar{N}L^3)^2$. The discrete nature of the source distribution means that in addition to the correlation term computed above, there will be a Poisson term. The Poisson contribution can be computed by considering the limiting case of equation (10) for a random source distribution and an experiment of infinite angular and spectral resolution,

$$C_l \simeq y^2 (\bar{N}L^3) \Delta\Omega_b \quad (11)$$

with y the average bubble distortion, $\bar{N}L^3$ the volume fraction occupied by bubbles and $\Delta\Omega_b$ their typical angular size. In practice, we find that the shot noise contribution is nearly always sub-dominant in the results we present below.

5. TOY MODEL FOR METAL DISTRIBUTION

To explore the detectability of the angular power spectrum of the OI-induced CMB distortion, we need a model for the spatial distribution of metals in the IGM. Following the discussion in § 3 and § 4 above, this means we need to specify the profile $W_b(r)$ around a halo of mass M at each redshift z .

Our basic simplifying assumption is that metals are confined in bubbles that had previously expanded into the IGM, but that these bubbles have settled to follow the Hubble flow. We assume that when a halo is formed, a metal-polluting wind is launched from the galaxy at the center of the halo, producing a bubble that subsequently expands at a constant velocity for the age of the halo. In principle, halos of the same mass that exist at a fixed redshift can have a distribution of ages. For simplicity, however, we assign a fixed age to halos of mass M at redshift z , corresponding to the average redshift z_f at which such halos assembled 65% of their mass (see, e.g., equation 2.26 in Lacey & Cole 1993). At redshift z , the radius of the bubble around a halo of mass M is therefore given by

$$L(M, z) = 0.1 r_{vir}(M, z_f) + (v_b^2 - v_{esc}^2)^{1/2} [t(z) - t(z_f)], \quad (12)$$

with r_{vir} the virial radius of the parent halo, and $t(z)$ the cosmic time at redshift z . The first term on the right hand side represents a rough estimate for the size of the galaxy in the halo (i.e., the region producing the metals). The velocity v_b , taken to be a constant in the range of $50 - 1500$ km s $^{-1}$, represents the wind velocity “in vacuum”. We then subtract v_{esc} , corresponding to the escape velocity from the parent halo at a distance of 0.1

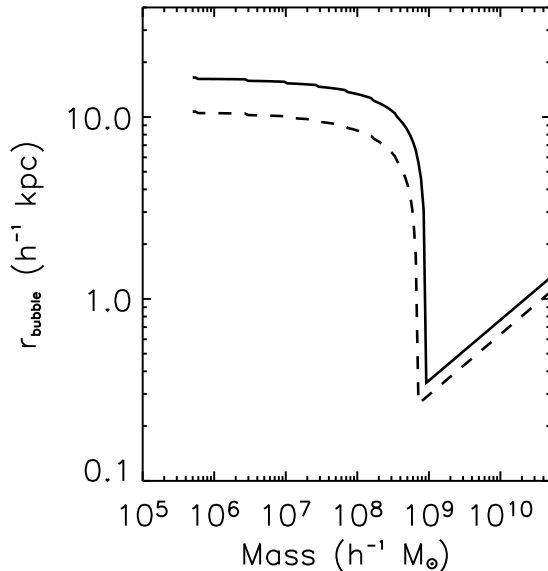


FIG. 2.— The radii of metal bubbles around halos of mass M produced in our fiducial toy-model, assuming metals expand over the typical age of the halo at a constant speed of $(v_b^2 - v_{esc}^2)^{1/2}$. Here v_b is a wind velocity equal to 150 km/s, and v_{esc} is the escape velocity from the halo. The solid curve shows the radii at $z = 6.5$; the dashed curve at $z = 7.5$. The sharp feature at $M \approx 10^9 M_\odot$ corresponds to the limit where metals are trapped inside the halo potential well ($v_b \approx v_{esc}$). The bubble radius for more massive halos is assumed to be a fixed fraction (here taken to be 10%) of the virial radius, and so it scales as $\propto M^{1/3}$.

$r_{vir}(M, z_f)$, from this wind velocity, to take into account the fact that metals lose energy as they travel out of the gravitational potential well. Since we assume that metals have no peculiar velocities, the bubbles start comoving with the Hubble flow by the time they are observed. Equation (12) assumes further that star-formation takes place instantly when the halo forms. In Figure 2, we show the bubble sizes predicted under these assumptions.

For simplicity, we normalize the total amount of oxygen mass in all bubbles at a given redshift by specifying the global average metallicity of the IGM at each redshift, i.e.,

$$Z_{av}(z) = \int_{M_{min}} dM \frac{dn}{dM}(M, z) Z(M, z) \mathcal{V}_b(M, z), \quad (13)$$

with $Z(M, z)$ the metallicity within a bubble at redshift z originated in a halo of mass M and with volume $\mathcal{V}_b = 4\pi/3 L^3$, and dn/dM is the halo mass function. For halos with $v_b > v_{esc}$, we further assume that, at a given redshift, the oxygen abundance within the bubble is proportional to the mass of the parent halo. Provided that the bubble radii are practically constant in this mass range, this is roughly equivalent to assuming that the star formation rate scales linearly with halo mass, and is constant throughout the age of the halo. For halos with $v_b < v_{esc}$, we assume that the oxygen density is constant (since the metals produced in these halos are assumed to be trapped in a volume $\mathcal{V}_b \propto M$); however, these larger halos contribute negligibly to the clustering signal below and our results are insensitive to this assumption.

In Figure 3, we show the evolution of the global average (dashed lines), and bubble-volume weighted (solid curves) metallicities versus redshift. The dotted curves show the fraction of the total volume contained inside the bubbles (note that metal-rich bubbles can overlap and this fraction can exceed unity). In all panels, the global average oxygen abundance is scaled to $10^{-2.5} Z_\odot$ at each redshift. This value is not unrealistic, as there are observational constraints on the cosmic metallicity indicating that $Z/Z_\odot \sim 10^{-3}$ at $z > 4$ (Schaye et al. 2003), and oxygen from first-generation stars is likely to be somewhat overabundant relative to the solar value (Meynet et al. 2006). The highest redshift, $z = 12$, shown in the figures represents the earliest epoch when this floor metallicity may have been established (e.g. Haiman & Loeb 1997). Note that since the global metallicity is re-scaled at each redshift by hand, the curves in Figure 3 should be interpreted as independent models of the metal distribution at each redshift, and not as evolutionary models. In order to illustrate the metal distribution under different assumptions, in panel (a), we assume $M_{min} = 5 \times 10^5 M_\odot$ and $v_b = 50$ km/s; panel (b) is the same as (a), except with $v_b = 150$ km/s, while in panel (c), we assume $v_b = 150$ km/s and $M_{min} = 5 \times 10^7 M_\odot$.

The enrichment scenarios considered in this work are comparable with those presented in previous studies. Indeed, in Furlanetto & Loeb (2003) the typical bubbles sizes at $z \sim 6$ are a few tens of kpc, in agreement with our estimates, whereas, after looking at the simulations of Oppenheimer et al. (2007), we have found similar enrichment levels in the relevant redshift ranges ($z \in [5, 10]$). Only in Scannapieco et al. (2002) the bubble filling factors tend to be slightly smaller than in our case, since, motivated by WMAP observations, we are considering early reionization models.

6. RESULTS AND DISCUSSION

The angular power spectrum (correlation term plus shot noise term) of the CMB distortion produced by the OI pumping is shown in Figure 4. We have adopted an angular resolution of one arc-second, and a relative spectral resolution of $\Delta\nu/\nu = 10^{-4}$. The angular resolution corresponds to $\ell \sim 7 \times 10^5$ and therefore should resolve all bubbles under consideration. The frequency resolution corresponds at $z = 6.5$ to roughly 60 kpc in physical units. In all three panels, we consider variations from our adopted fiducial model given by $z = 6.5$ (observable at 630 GHz), $I_\nu^{20} = 6 \times 10^{-20} \text{ erg cm}^{-2} \text{ s}^{-1} \text{ Hz}^{-1} \text{ sr}^{-1}$, $M_{min} = 5 \times 10^5 M_\odot$, and $v_b = 150$ km/s, corresponding to $L \simeq 60$ kpc at that redshift. Panel (a) shows the dependence of the signal on bubble expansion velocity/bubble size: 150 (solid curve), 60 (dashed curve), and 200 (dotted curve) km/s, which correspond to $L \simeq 60$, 23 and 80 kpc respectively. If $v_b = 60$ km/s ($L \simeq 23$ kpc), then $L < cH^{-1}(z_s)\Delta\nu_{th}/\nu_{10}$, and the bubbles remain optically thin (y has not reached its maximum value), so that $(l^2 C_l)_{max} \propto \mathcal{G}^2 L^2$. On the other hand, for $v_b \sim 150$ km/s ($L \simeq 60$ kpc), we are in the regime of $L \gtrsim cH^{-1}(z_s)\Delta\nu_{th}/\nu_{10}$ and $(l^2 C_l)_{max} \propto \mathcal{G}^2$. Therefore, if $v_b = 200$ km/s, the amplitude of the spectrum should not change noticeably. However, the bubble size ($L \simeq 80$ kpc) is slightly larger than in our fidu-

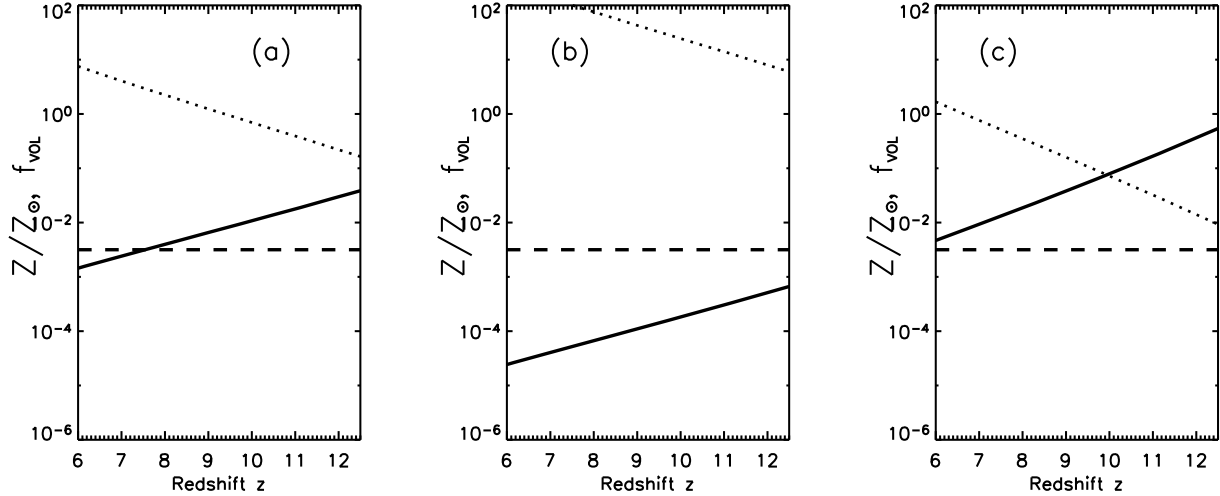


FIG. 3.— Models of metal enrichment in the IGM at various redshifts. The global average metallicity Z/Z_{\odot} is shown by the dashed curves, and the metallicity inside individual metal bubbles by the solid curves. Note that the global metallicity is renormalized at each redshift by hand to the same metallicity, and the curves should not be interpreted as evolutionary models. The dotted curves show the volume-filling fraction occupied by bubbles (note that metal-rich bubbles can overlap and this fraction can exceed unity). Panel (a): $M_{\min} = 5 \times 10^5 M_{\odot}$, $v_b = 60$ km/s and global average $Z/Z_{\odot} = 10^{-2.5}$ set to a constant in redshift. At $z \simeq 6.5$ the typical bubble size is $L \sim 22$ kpc, and bubbles have been generated in halos of typical mass $M \sim 4 \times 10^6 M_{\odot}$. Panel (b): same as panel (a) but $v_b = 150$ km/s, which corresponds, at $z \simeq 6.5$, to a typical bubble size of $L \sim 60$ kpc. Panel (c) $v_b = 150$ km/s (corresponding to $L \sim 50$ kpc at $z \simeq 6.5$) and $M_{\min} = 5 \times 10^7 M_{\odot}$.

cial model ($L \simeq 60$ kpc), and when comparing both cases one can clearly see the effect of the bubble window function suppressing power at small scales. Therefore $(l^2 C_l)_{\max} \propto (v_b/150 \text{ km/s})^2$ if $v_b < 150$ km/s. In panel (b), we find a strong dependence of the power on the redshift: for the range of $z_s = 6.5, 7, 7.5$ (from top to bottom), the amplitude of the power spectrum varies by nearly two orders of magnitude. This steep dependence arises because the efficiency of the pumping is exponentially dependent on the difference between the CMB and the spin temperatures, and this difference is reduced at higher z (see Paper I for more discussion).

Panel (c) in Figure 4 shows the dependence on the minimum size of the halo producing metal-bubbles, with $M_{\min} = 5 \times 10^5$ (solid line), 5×10^8 (dashed line), and $7.5 \times 10^8 M_{\odot}$ (dotted line). This roughly brackets the possible range of minimum halo sizes, based on the presence or absence of H_2 molecules (e.g. Haimes et al. 1997). At $M_{\min} = 5 \times 10^5 M_{\odot}$, $L \sim cH^{-1}(z_s)\Delta\nu_{th}/\nu_{10}$, which would yield the scaling $(l^2 C_l)_{\max} \propto \mathcal{G}^2$, i.e., independent on M_{\min} . However, the actual amplitude does vary with mass in the range of $5 \times 10^5 M_{\odot} < M_{\min} < 7.5 \times 10^8 M_{\odot}$ due to several reasons. First, increasing the halo mass results in a larger bias factor (from $b \simeq 1.4$ to $b \simeq 2.6$). Second, at large M_{\min} , there are fewer bubbles per unit volume, assumed to contain the same amount of metals, so the bubbles become optically thick, and $y \sim \mathcal{G}$ and $(l^2 C_l)_{\max} \propto \mathcal{G}^2 (\bar{N}L^3)^2$. But most importantly, for $M_{\min} > 5 \times 10^8 M_{\odot}$, the typical bubble radii (and corresponding volumes) shrink considerably (c.f. Fig. 2), and due to the scaling $C_l \propto (\bar{N}L^3)^2$, this causes a correspondingly steep drop in the power amplitude (dotted line in Fig. 4c)). We also note that for the largest minimum mass considered, the shot noise contribution starts dominating at the smallest scales. We find that the amplitude of the signal depends strongly on the parameters

of the model. However, the toy model for the metal distribution was introduced only to gain insight on the nature of the signal and should be regarded as a toy model. Numerical simulations with radiative transfer should be used to make more quantitative predictions and will be crucial in the interpretation of future observations.

The multipole corresponding to $(l^2 C_l)_{\max}$ in Figure 4 is related to the projected k mode at which the convolved matter power spectrum peaks. In principle, the typical bubble clustering length could also be detected in the *radial* direction if the observing instrument had enough spectral resolution: in such case, observations at slightly different frequencies would give rise to *correlated* maps, since they would be probing overlapping shells centered at similar redshifts. The combination of maps obtained at different frequencies could also improve the S/N ratio of the final detection.

Because at the frequencies of interest the signal will be dominated by infrared emission from dusty galaxies, it is important to be able to remove them from the observed map. One way this can be achieved is by obtaining high angular resolution images of the sky at the frequencies of interest, so that Olber's paradox is avoided and individual galaxies can be clipped from the maps. The Atacama Large Millimeter Array (ALMA) may be an excellent instrument for this purpose because of its high sensitivity and angular resolution (of the order of $0.5''$). The drawback is that the field of view of ALMA is small ($\lesssim 1$ arcmin). However, since our signal peaks at scales of \sim tens of arcseconds and decays slowly at smaller scales, this small field of view should not be a fundamental limitation. The signal could also be within reach of the sensitivity of forthcoming detectors (e.g., SCUBA2, (Holland et al. 2006)) and of planned single dish experiments such as

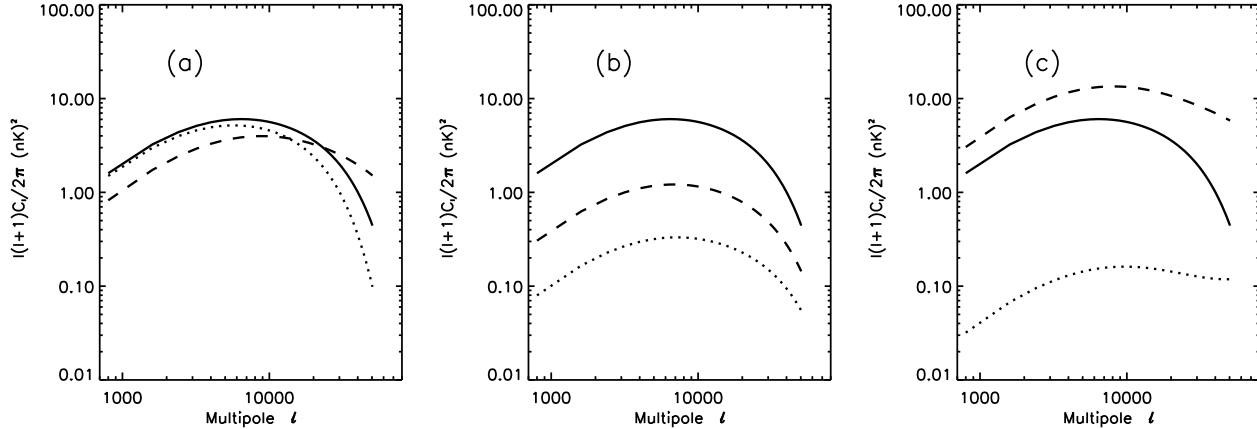


FIG. 4.— The dependence of the angular fluctuation power, $l^2 C_l$, on metal distribution model parameters and on redshift. In all three panels, we display our adopted fiducial model given by: $z = 6.5$ (observable at 630 GHz), $I_{\nu}^{20} = 6 \times 10^{-20} \text{ erg cm}^{-2} \text{ s}^{-1} \text{ Hz}^{-1} \text{ sr}^{-1}$, $M_{\min} = 5 \times 10^5 M_{\odot}$ and $L \simeq 60 \text{ kpc}$. Panel (a): dependence of the signal on bubble size: 23, 60, 80 kpc for the dashed, solid and dotted curve, respectively. For $L \simeq 23 \text{ kpc}$ we still have $L < cH^{-1}(z_s)\Delta\nu_{th}/\nu_{10}$ and the scaling changes to $(l^2 C_l)_{\max} \propto \mathcal{G}^2$. The dotted line ($L \simeq 80 \text{ kpc}$) shows how power is suppressed in scales below the typical bubble size. Panel (b): dependence of the signal on redshift: $z = 6.5, 7, 7.5$ from top to bottom, corresponding to observing frequencies $\nu = 633, 593$ and 558 GHz , respectively. Panel (c): dependence on the minimum halo mass: $M_{\min} = 5 \times 10^5$ (solid line), 5×10^8 (dashed line), and $7.5 \times 10^8 M_{\odot}$ (dotted line). The distortion y becomes saturated for $M_{\min} \gtrsim 5 \times 10^8 M_{\odot}$. For $5 \times 10^5 M_{\odot} < M_{\min} < 5 \times 10^8 M_{\odot}$, we have the approximate scaling $(l^2 C_l)_{\max} \propto \mathcal{G}^2$ that is slightly distorted by the presence of the bias factor enhancing the dashed curve over the solid one. For $M_{\min} = 7.5 \times 10^8 M_{\odot}$ we are well in the optically thick regime ($C_l \propto (\bar{N}L^3)^2$) and the typical bubble sizes have shrunk dramatically (see Fig. 2; this translates into a clear drop in the power (thinnest curve).

CCAT⁶. However, current small scale CMB experiments, with a typical sensitivity of $\sim \mu\text{K}$ at arcmin scales, are still rather far from imposing interesting constraints on this effect.

7. CONCLUSIONS

In this paper, we have computed the angular fluctuation of the effect we presented in an earlier work (Paper I): the CMB spectral distortion induced by OI 63.2 μm fine transition, pumped at the epoch of reionization by the UV background radiation via the OI Balmer α line. Since the oxygen distribution in space is associated with the most over-dense regions hosting the first star forming activity at the end of the Dark Ages, there must be fluctuations in the angular pattern of the OI-induced y distortion. We have considered the clustering properties of the signal and computed its angular power spectrum using a toy model for the metal distribution. We find that the predicted signal is small, but that

for certain enrichment models it could be detected using ultra-deep observations with a sensitive instrument such as ALMA, SCUBA2 and CCAT. Even in the event of a non-detection, future infrared observations could place interesting limits on the metal enrichment of the universe during the Dark Ages. This could open the possibility of measuring the metal enrichment of the universe before it was re-ionized. OI observations would also be complementary to HI 21cm measurements that will map out in the near future the distribution of neutral H during the epoch or re-ionization.

ZH acknowledges partial support by NASA grant NNG04GI88G. CHM, LV and RJ acknowledge support by NASA grant ADP04-0093, and NSF grant PIRE-0507768. The authors thank Chris Carilli for useful discussions.

⁶ CCAT URL site: <http://www.submm.org>

REFERENCES

- Basu, K., Hernández-Monteagudo, C., & Sunyaev, R. A. 2004, A&A, 416, 447
 Becker, G. D., Sargent, W. L. W., Rauch, M., & Simcoe, R. A. 2006, ApJ, 640, 69
 Dijkstra, M., Wyithe, J. S. B., & Haiman, Z. 2007, MNRAS, 379, 253
 Fan, X., Carilli, C. L., & Keating, B. 2006, ARA&A, 44, 415
 Fixsen, D. J., & Mather, J. C. 2002, ApJ, 581, 817
 Furlanetto, S. R., & Loeb, A. 2003, ApJ, 588, 18
 Haiman, Z., Rees, M. J., & Loeb, A. 1997, ApJ, 476, 458 [erratum: 1997, ApJ, 484, 985]
 Haiman, Z., & Loeb, A. 1997, ApJ, 483, 21
 Heger, A., & Woosley, S. E. 2002, ApJ, 567, 532
 Hernández-Monteagudo, C., Verde, L., & Jimenez, R. 2006, ApJ, 653, 1
 Hernández-Monteagudo, C., Haiman, Z., Jimenez, R., & Verde, L. 2007, ApJ, 660, L85 (Paper I)
 Holland, W., et al. 2006, Proc. SPIE, 6275,
 Iliev, I. T., Scannapieco, E., Martel, H., & Shapiro, P. R. 2003, MNRAS, 341, 81
 Kashikawa, N., et al. 2006, ApJ, 648, 7
 Kogut, A., et al. 2003, ApJS, 148, 161
 Lacey, C., & Cole, S. 1993, MNRAS, 262, 627
 Malhotra, S., & Rhoads, J. E. 2006, ApJ, 647, L95
 McQuinn, M., Hernquist, L., Zaldarriaga, M., & Dutta, S. 2007, ArXiv e-prints, 704, arXiv:0704.2239
 Meynet, G., Ekström, S., & Maeder, A. 2006, A&A, 447, 623
 Oh, S. P. 2002, MNRAS, 336, 1021
 Oh, S. P., Cooray, A., & Kamionkowski, M. 2003, MNRAS, 342, L20
 Oh, S. P. & Haiman, Z. 2003, MNRAS, 346, 456

- Oppenheimer, B. D., Davé, R., & Finlator, K. 2007, EAS Publications Series, 24, 157
- Furlanetto, S. R., Oh, S. P., & Briggs, F. H. 2006, Phys. Rep., 433, 181
- Page, L., et al. 2007, ApJS, 170, 335
- Scannapieco, E., Ferrara, A., & Madau, P. 2002, ApJ, 574, 590
- Schaye, J., Aguirre, A., Kim, T.-S., Theuns, T., Rauch, M., & Sargent, W. L. W. 2003, ApJ, 596, 768
- Sheth, R. K., & Tormen, G. 1999, MNRAS, 308, 119
- Sheth, R. K., & Tormen, G. 2004, MNRAS, 349, 1464
- Spergel, D. N., et al. 2007, ApJS, 170, 377
- Sunyaev, R. A. & Zeldovich, I. B. 1980, ARA&A, 18, 537
- Totani, T., Kawai, N., Kosugi, G., Aoki, K., Yamada, T., Iye, M., Ohta, K., & Hattori, T. 2006, PASJ, 58, 485
- Wouthuysen, S. A. 1952, AJ, 57, 31